

Quantitative assessments of geometric errors for rapid prototyping in medical applications

Cristobal Arrieta

Department of Electrical Engineering and Biomedical Imaging Center, Pontificia Universidad Catolica de Chile, Santiago, Chile

Sergio Uribe

Biomedical Imaging Center and Radiology Department, Pontificia Universidad Catolica de Chile, Santiago, Chile

Jorge Ramos-Grez

Department of Mechanical and Metallurgical Engineering, Pontificia Universidad Catolica de Chile, Santiago, Chile

Alex Vargas

Department of Surgery, Pontificia Universidad Catolica de Chile, Santiago, Chile, and

Pablo Irarrazaval, Vicente Parot and Cristian Tejos

Department of Electrical Engineering and Biomedical Imaging Center, Pontificia Universidad Catolica de Chile, Santiago, Chile

Abstract

Purpose – In medical applications, it is crucial to evaluate the geometric accuracy of rapid prototyping (RP) models. Current research on evaluating geometric accuracy has focused on identifying two or more specific anatomical landmarks on the original structure and the RP model, and comparing their corresponding linear distances. Such kind of accuracy metrics is ambiguous and may induce misrepresentations of the actual errors. The purpose of this paper is to propose an alternative method and metrics to measure the accuracy of RP models.

Design/methodology/approach – The authors propose an accuracy metric composed of two different approaches: a global accuracy evaluation using volumetric intersection indexes calculated over segmented Computed Tomography scans of the original object and the RP model. Second, a local error metric that is computed from the surfaces of the original object and the RP model. This local error is rendered in a 3D surface using a color code, that allow differentiating regions where the model is overestimated, underestimated, or correctly estimated. Global and local error measurements are performed after rigid body registration, segmentation and triangulation.

Findings – The results show that the method can be applied to different objects without any modification, and provide simple, meaningful and precise quantitative indexes to measure the geometric accuracy of RP models.

Originality/value – The paper presents a new approach to characterize the geometric errors in RP models using global indexes and a local surface distribution of the errors. It requires minimum human intervention and it can be applied without any modification to any kind of object.

Keywords Rapid prototyping, Volume measurement, Image processing, Geometric accuracy, Volumetric accuracy indexes

Paper type Research paper

1. Introduction

Rapid prototyping (RP) is a technique that was introduced in mechanical engineering for producing three-dimensional (3D) physical models of objects. RP is used in medical applications to construct realistic replicas of biological structures (also known as RP models), being the most common application the construction of bone models. RP models have been used for surgical planning, prosthesis design, assisted diagnosis, and teaching purposes (Choi *et al.*, 2002; Silva *et al.*, 2008; Schicho *et al.*, 2006; Russett *et al.*, 2007; Ngan *et al.*, 2006).

The construction of RP models typically consists of four steps (Figure 1):

- 1 The object is scanned using a volumetric medical imaging technique, usually computed tomography (CT) or magnetic resonance imaging.
- 2 The object of interest is segmented out from the acquired image.
- 3 The surface of the segmented object is triangulated to generate a piece-wise continuous surface model, which is then exported into an STereoLithography (STL) file.
- 4 The model is built from the STL file using one of the existing RP techniques.

Unfortunately, each step of this process introduces several errors (e.g. voxelation, segmentation errors, piecewise linear smoothing by the triangulation, deformations due to calibration errors of the manufacturing system), so the resulting RP model is not geometrically identical to the object.

The current issue and full text archive of this journal is available at www.emeraldinsight.com/1355-2546.htm

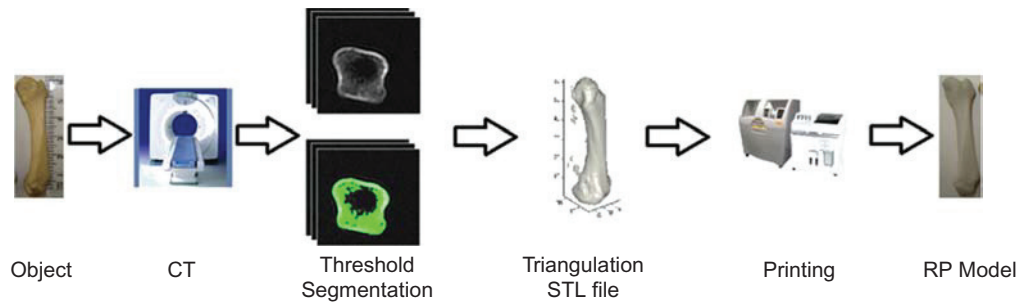


Rapid Prototyping Journal
18/6 (2012) 431–442
© Emerald Group Publishing Limited [ISSN 1355-2546]
[DOI 10.1108/13552541211271974]

This work has been supported by Fondecyt 1100864, Anillo ACT79 and Fondef D06I 1026.

Received: 20 January 2011
Accepted: 7 May 2011

Figure 1



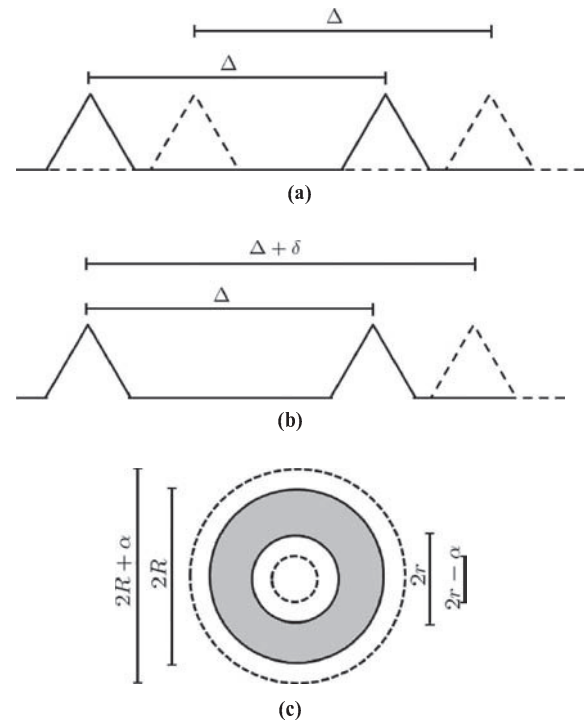
The accuracy of RP models is crucial in medical applications, hence, having a reliable error metric is essential to evaluate the final product. Most of the documented methods use linear distances between anatomical landmarks to quantify these geometric errors (Choi *et al.*, 2002; Silva *et al.*, 2008; Schicho *et al.*, 2006; Russett *et al.*, 2007; Nizam *et al.*, 2006; Knox *et al.*, 2005; El-Katatny *et al.*, 2010). For example, Choi *et al.* (2002) implemented a procedure by identifying two or more relevant anatomical landmarks and locating them on the object and on the corresponding places in the RP model. They measured the linear distances between landmarks in the object and compared these distances to the ones obtained from the RP model.

Despite their extensive use, methods that use landmarks to quantify geometric errors have three disadvantages.

First, they require an experienced person who needs to identify manually and precisely a set of relevant anatomical features for the specific object. There are significant intra- and inter-observer differences placing the landmarks. In order to alleviate intra-observer effects, Choi *et al.* (2002) and Silva *et al.* (2008) needed to average over 20 different distance measurements of each landmark pair in their RP accuracy studies. Malleprey and Bergers (2009) proposed a method to quantify the accuracy of RP models that uses a coordinate measuring machine (CMM) to measure 23 landmark pairs with six iterations per measurement. CMM significantly improves the accuracy of measuring spatial coordinates of specific points, and allows comparing precisely the location of the selected landmarks. However, those landmarks still need to be located (with a probe) by a human operator and consequently, the process is still prone to have inter- and intra-observer variability. As any point-based approach, CMM-based methods do not offer a dense amount of data to analyze the entire surface. Elkott and Veldhuis (2007) showed that the point sampling rate could be increased using continuous-contact probing systems, which allow acquiring dense data along a curved path traced by the user. Importantly, CMM can only measure external surfaces strictly convex or with minor concavities, otherwise there are regions that cannot be reached by the CMM probe. This is an important restriction for *in vivo* medical applications since there are several inner surfaces that may need to be evaluated (e.g. when measuring the thickness of the skull).

Second, even if landmarks were perfectly located, error metrics based on linear distances would still suffer from inherent ambiguities and could lead to wrong conclusions when they are used to quantify volumetric errors. Figure 2 shows some examples of these ambiguities. For instance, if in the RP model two landmarks are erroneously displaced in the same

Figure 2



direction and same magnitude with respect to the original object (Figure 2(a)), the distance between them would not change, so no error would be detected. Alternatively, if only one landmark is misplaced (Figure 2(b)), the method would detect an error, but without identifying which landmark is in the wrong position. Another ambiguity occurs depending on where the RP model is measured. For instance, an overestimated doughnut-like object (Figure 2(c)) would present an increased linear distance ($2R + \alpha$) in the outer diameter, whereas the inner diameter would show a decreased linear distance ($2r - \alpha$), despite of the underlying geometric error being the same.

Third, when landmark-based methods are used to encode global geometric errors (i.e. a number that represents the total error of the RP model), the common approach is to take the mean and standard deviation of the differences between an arbitrarily chosen number of landmark distances. This produces an uneven comparison between different objects since the number of landmarks tends to vary across objects.

In summary, landmark-based methods have intrinsic and inevitable ambiguities, and result in error estimates that,

depending on the object, the type of distortions and the number of measurements, could be inaccurate.

Germani *et al.* (2010), Wang *et al.* (2010), Ciocca *et al.* (2009) and Meakin *et al.* (2004), used a slightly different accuracy evaluation method that considers a colored surface representation to show local errors of the RP models. In general, this approach consists of taking two point clouds (one from the surface of the evaluated object and another from the RP model), finding the overlapped region and computing the magnitude of the distance between each point of one cloud to the nearest point of the other cloud. The surface of the object is then rendered using different colors that encode the computed distances. Despite of providing a notion of the surface local errors, this approach does not give any information about the error direction. Thus, one cannot discriminate overestimated from underestimated surfaces.

Considering these issues, we propose new metrics and a novel method to estimate geometric errors of RP models based on image processing techniques. In our approach we use two metrics to evaluate independently the global error (indexes that represent the total error of the RP model) and local errors (error distribution along the surface of the RP model). For global accuracy, we propose to use volumetric intersection indexes computed over scans of the object and the RP model. The purpose of this is twofold: to provide a more accurate measure of error by simple and meaningful indexes that take into account volumes, avoiding thus the ambiguities present in methods based on linear distances; and to privilege automation, as only little human intervention is needed. For local accuracy, we propose to use a 3D surface map with a color code that indicates if each region of the RP model overestimates, underestimates, or correctly estimates the surface of the original object. Furthermore, by means of an intensity code, we are able to quantify the local error in each region of the RP model.

2. Materials and methods

In this section, we present our method for the analysis of geometric errors in RP models. First, we show how the RP models were constructed from cadaveric bones and from phantoms in which we controlled the geometric errors. Second, we describe the different steps to acquire and process the data. Finally, we present how the global and local metrics are computed.

2.1 RP models construction

We generated two analytical phantoms, designed with the software CATIA™ v5 R14 (Dassault Systèmes, Vélizy-Villacoublay, France):

- 1 a sphere with radius 2.5 cm (Figure 3(a)); and
- 2 a sphere with the same radius with two cylindrical defects, one of them added volume (Figure 3(b)) and the other subtracted the same volume (Figure 3(c)), so as to keep the same volume of the original sphere.

The radius of both cylinders was 0.7 cm. The height of one of them was 1 cm and we found the other height by preserving the sphere volume, resulting in a slightly smaller height. The added and subtracted volumes were equal to 1.478 cm³, i.e. 2.26 percent of the total volume.

We also built RP models of cadaveric bones obtained from the Department of Anatomy of our university. For our experiments we used five bones: a humerus portion,

an ulna, and three metacarpal bones. Two examples are shown in Figure 4.

The RP models were constructed from CT scans (GE HiSpeed Dual) obtained with the following parameters: 80 kV, 80 mA, matrix resolution of 512 × 512 and slice thickness of 1 mm. The field of view was adjusted on each experiment so that to optimize the in-plane image resolution. Data were processed using a standard software application for RP models (Mimics™ 12, Materialise®, Leuven, Belgium). This software had a manual thresholding-based segmentation and some basic region growing-based tools to edit the results of the segmentation. From this segmentation, the software generated a triangulated surface using the following parameters: in-plane resolution and thickness identical to those from the CT scan; two iterations of smoothing with a smooth factor of 0.3; triangle reduction using advanced edge mode, using a tolerance of 0.0122 mm, edge angle of 10° and three iterations. The triangulation, saved as an STL file, was exported into a ZPrint™ software. Subsequently, the data were re-sliced with resolution of 0.089 mm and built in the same slice direction of the CT, using a ZPrinter™ Spectrum 510 system (ZCorporation, Franklin, Massachusetts, USA), with a resolution of 600 × 540 dpi. For our experiments, the RP models were not infiltrated.

To run blind experiments, an independent operator performed the whole RP building process of all the studied objects. This operator did not participate in the evaluation process, which will be described in the following sections.

2.2 Data processing of RP models

Our proposed accuracy metrics were computed after the following image processing steps (Figure 5). Once the RP model was built, we performed a CT scan of it using the same parameters previously defined for the CT of the object. We used these parameters as they showed the best results in terms of image quality. At this point we had two sets of medical images, one from the object and another from the RP model.

In order to have voxel-to-voxel spatial correspondence, we registered both CTs using a rigid body algorithm based on mutual information (Wells *et al.*, 1996) available in the software application SPM (www.fil.ion.ucl.ac.uk/spm accessed on 11 January 2011). The registered images were segmented using a 3D active contour without edges (ACWE) algorithm (Chan and Vese, 2001) implemented in a home-made application using MATLAB 7.8.0 (Mathworks, Natick, Massachusetts, USA). This is a level set-based segmentation technique, which is formulated using a Mumford and Shah (1989) functional. Basically, the idea of the algorithm is to evolve an interface that divides the image into two homogeneous regions. This is solved minimizing the energy functional:

$$\begin{aligned}
 F(c_1, c_2, C) = & \mu \cdot Area(C) + \nu \cdot Volume(inside(C)) \\
 & + \lambda_1 \int_{inside(C)} |u_0(\vec{x}) - c_1|^2 d\vec{x} \\
 & + \lambda_2 \int_{outside(C)} |u_0(\vec{x}) - c_2|^2 d\vec{x}
 \end{aligned} \quad (1)$$

where C corresponds to the surface that describes the interface, $u_0(\vec{x})$ corresponds to the 3D image, c_1 and c_2 are the average intensity of $u_0(\vec{x})$ inside and outside of C , respectively. Additionally, μ , ν , λ_1 and λ_2 are fixed parameters chosen by

Figure 3

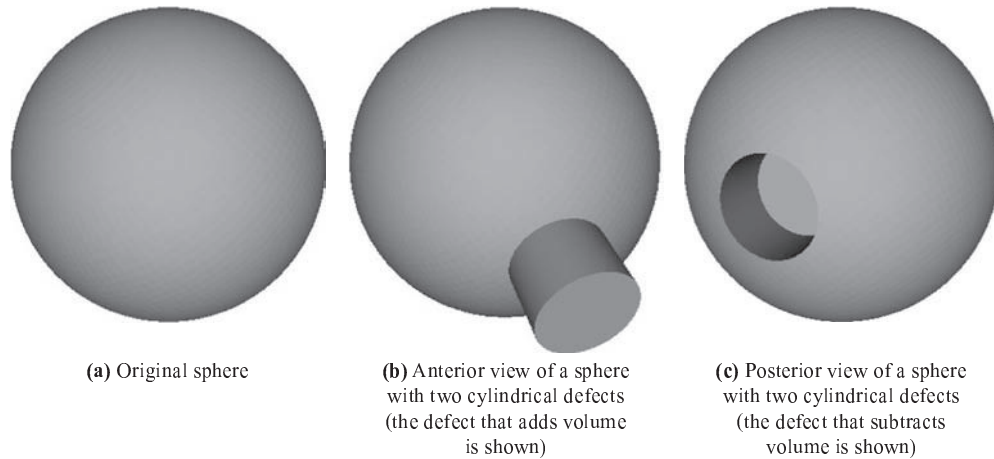


Figure 4



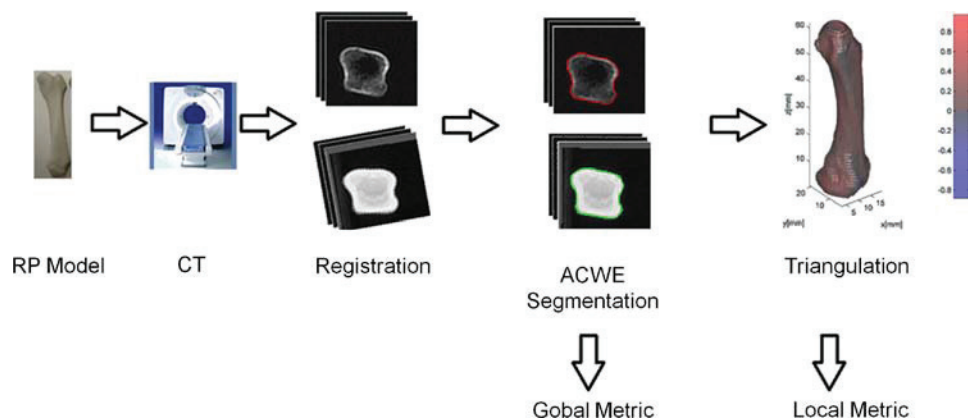
the user and they represent the weights of each term in the objective function. The first term of the equation (1) forces the surface C to be smooth. The second term minimizes the volume inside C , but having a minimal volume is not usually desired so typically $\nu = 0$. The third and fourth terms force C to be located such that the interior and exterior regions are, respectively, as homogeneous as possible.

The minimization of equation (1) is achieved by an iterative method (Chan and Vese, 2001) consisting of a finite difference discretization in the spatial domain and a forward Euler time discretization which adds a Δt parameter that represented the size of one time step of this method.

After a few tests in one slice of a bone and RP model, we set the parameters as: $\mu = 0.01 \times 255^2$, $\nu = 0$, $\lambda_1 = 1$, $\lambda_2 = 7$ (bone), $\lambda_2 = 1$ (RP model), $\Delta t = 0.01$, 300 iterations, nine iterations of re-initialization after the first iteration and then every 101 iterations. We kept these parameters constant for all our experiments. The only human intervention was the initialization process, which consisted in defining an ellipsoid that surrounded the entire object of interest. Once the segmentation process ended, automatic morphological operations were needed to extract only the exterior surface of the object.

Finally, we generated a triangulated surface of both data sets using the marching cubes algorithm (Lorenson and Cline, 1987). This algorithm analyzes the cubes formed by an eight-point neighborhood of each voxel and assigns a binary value to each vertex of the cube depending on whether it belong to the object or to the background. There are 256 possible cases for a cube and each of them corresponds to a pattern of how a single or a set of triangles can intersect the cube. Actually, only 14 triangular patterns are needed, since the rest can be

Figure 5



obtained rotating or reflecting the triangles. The resulting triangulations were then exported into an STL file.

2.3 Global accuracy metrics

Using the segmented images from the object and the RP model we analyzed the global geometric error using three indexes (Figure 6). The first index, A , was the normalized intersection between voxels that belong to the object segmentation (V_b) and to the RP model segmentation (V_m) (gray voxels in Figure 6):

$$A = \frac{\sum(V_b \cap V_m)}{\sum V_b} \cdot 100 \quad (2)$$

We defined the normalized false positive (FP) error, i.e. voxels that appear in the RP model segmentation but not in the object segmentation (\tilde{V}_b) (pink voxels in Figure 6), as:

$$FP = \frac{\sum(\tilde{V}_b \cap V_m)}{\sum V_b} \cdot 100 \quad (3)$$

and the normalized false negative (FN) error, i.e. voxels that appear in the object segmentation but not in the RP model segmentation (\tilde{V}_m) (purple voxels in Figure 6), as:

$$FN = \frac{\sum(V_b \cap \tilde{V}_m)}{\sum V_b} \cdot 100 \quad (4)$$

2.4 Local accuracy metric

Using the surface triangulation (STL file) of the object and the RP model, we analyzed the local geometric errors. The idea was to have an indication of how far apart were those surfaces. We compared both triangulations computing a *signed normal distance* of each triangle of the object to the nearest triangle of the STL file of RP model. The surface of the model could be overestimated (positive distance), underestimated (negative distance), or well-estimated (zero distance). Each of these classifications had a corresponding color: pink tones for FP , purple tones for FN , and gray for well-estimated regions. Then, the intensity was associated with the magnitude of the signed normal distance. That information was rendered in a 3D surface representation of the original object.

Figure 7 shows a general case, in which the object triangulation is represented by the green triangle and the RP model triangulation is represented by yellow triangles. We compute the signed normal distance between each object's triangle (computed from the incenter \vec{I}_s) and the intersection point (\vec{P}) of the nearest RP model triangle, represented in blue. To compute the signed normal distances we proceeded as follows:

Figure 6

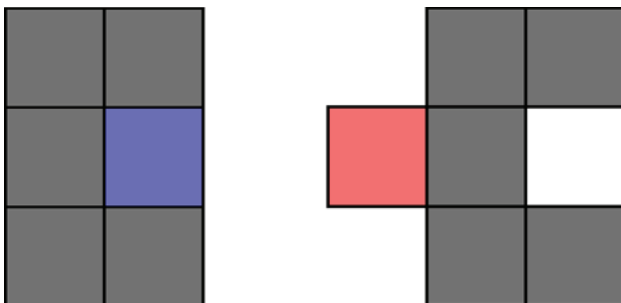
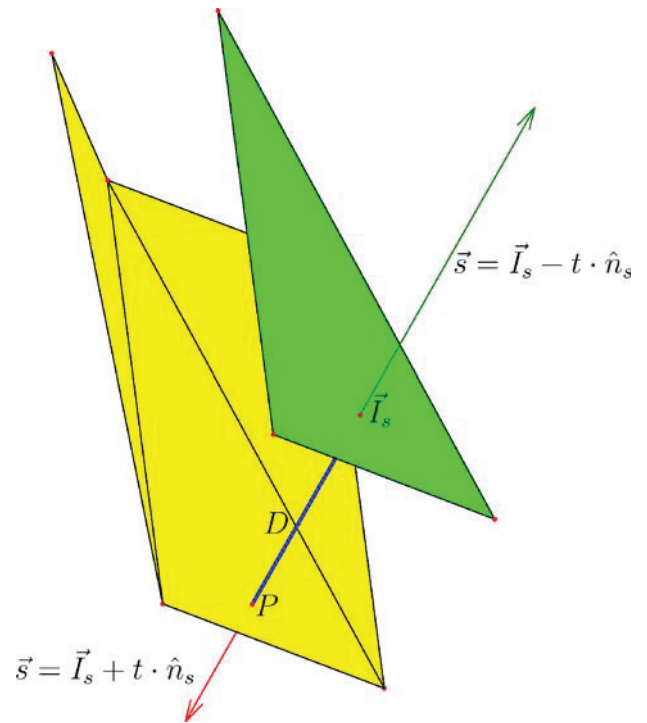


Figure 7



- 1 Compute \vec{I}_s and \vec{I}_m , the triangle incenters of the object and RP model STLs, respectively.
- 2 Compute \hat{n}_s and \hat{n}_m , the unit outer normal of the triangles of the STL file of the object and RP model, respectively.
- 3 Compute the plane that contains each triangle of the STL file of RP model as:

$$ax + by + cz + d = 0 \quad (5)$$

where a , b and c are known since $\hat{n}_m = (a, b, c)$ and d is defined as:

$$d = -\hat{n}_m \cdot \vec{I}_m \quad (6)$$

where \cdot is the dot or inner product.

- 4 Define \vec{s} , the normal straight line of each triangle of the STL file of the object through \vec{I}_s as:

$$\vec{s} = \vec{I}_s + t \cdot \hat{n}_s \quad (7)$$

where t is a free parameter.

- 5 Compute the intersection point P between \vec{s} and the plane that contains each triangle of the STL file of RP model. This can be done evaluating equation (7) with t equals to:

$$t = \frac{-d - \vec{I}_s \cdot \hat{n}_m}{\hat{n}_s \cdot \hat{n}_m} \quad (8)$$

- 6 Keep the intersection points P that belong to the interior of any triangle of the STL file of RP model and discard the rest. We considered that edges and vertices belonged to the interior of the triangles.
- 7 Compute the signed normal distances as:

$$D = \|\vec{I}_s - P\| \cdot \text{sign}(t) \quad (9)$$

where $\|\cdot\|$ is the Euclidean distance, $\text{sign}(t) = 1$ denotes an outer normal direction and $\text{sign}(t) = -1$ denotes an inner normal direction.

- 8 As each \vec{s} usually intersects more than one triangle, we simply chose the distance D with the smallest magnitude (D_m). At this stage, each triangle of the STL file of the object has a corresponding signed normal distance D_m .
- 9 Generate a color code of 256 levels to show each D_m with a corresponding color. The red, green and blue (RGB) channels of the color code were defined as follows:
 - Find the level that corresponds to the zero distance with the proportion:

$$p = \text{floor} \left(256 \cdot \frac{|\min(\vec{D}_m)|}{|\min(\vec{D}_m)| + |\max(\vec{D}_m)|} \right)$$

where \vec{D}_m is the vector that contains the signed normal distances of all the triangles that belong to the object and the function *floor* rounds to the nearest integers towards minus infinity.

- The p th element, corresponding to the zero signed normal distance, was defined as gray RGB = [0.45 0.45 0.45]. We needed that the colormap gradually changes its color for negative and positive distances, so we assigned the blue channel for the negative distances and the red channel for the positive distances.
- For negative distances we kept the red channel equal to 0.45 and we defined the 256 elements of the blue channel using:

$$B(i) = \begin{cases} \frac{0.55}{\min(D_m)} + 0.45 & i = 1, \dots, p \\ 0.45 & i = p + 1, \dots, 256 \end{cases} \quad (10)$$

- For positive distances we kept the blue channel equal to 0.45 and we defined the red channel using:

$$R(i) = \begin{cases} 0.45 & i = 1, \dots, p - 1 \\ \frac{0.55}{\max(D_m)} + 0.45 & i = p, \dots, 256 \end{cases} \quad (11)$$

- The green channel of the colormap was $G = 0.45$ for all values. Different color codes can be constructed by simply adjusting the coefficients of the straight lines defined in equations (10) and (11).

3. Results

3.1 Phantom results

Figure 8 shows the result of the registration and the ACWE segmentation of the original sphere and the sphere with cylindrical defects. Figure 8(c) shows the superposition of the segmentation represented by contours.

The segmentation algorithm based on ACWE worked equally well on the original sphere (red contour in Figure 8(a)) and on the sphere with defects (green contour in Figure 8(b)). By superposing both segmentations together (red and green contours) onto the CT of the original sphere (Figure 8(c)), it can be seen that there was no substantial differences between them, except in the region of the introduced defect.

The global accuracy indexes of the spheres were: $A = 97.17$ percent, $FP = 2.48$ percent, and $FN = 2.83$ percent, whereas the expected indexes were 97.74 percent and $FP = FN = 2.26$ percent.

The local error is shown in Figure 12(a). The region in red represents the introduced *FP* cylinder defect. The maximum and minimum signed normal distances were about 6 and -6 mm, respectively.

3.2 Bone results

As can be seen from Figures 9 and 10, the registration and segmentation worked well for all CT scans (only one slice of two experiments are shown). Figure 11 shows the global errors of each bone. It can be seen that there was a slight geometric error in the RP models, as there was a consistent overestimation in their sizes. Indeed, the amount of *FPs* was greater than the amount of *FNs*, except for the metacarpal 3.

These percentages of *FP* and *FN* (Figure 11) represent the global accuracy of RP models but they do not show information about where these errors are located. Figure 12 shows our local error representation. As previously stated, pink tones represented overestimated regions (*FP*), purple tones represented the underestimated regions (*FN*) and gray tones represented the correctly estimated regions. Except for the metacarpal 3, the rendered surfaces showed mostly *FP* errors. This was consistent with the computed global indexes. Interestingly, the maximum deviation of *FP* was less than the maximum deviation of *FN* (see the colorbars in Figure 12). Moreover, in general *FN* were concentrated on specific zones of the surface. The result of the metacarpal 3 was different since *FP* and *FN* were equally distributed along the surface, which was also consistent with the global error results.

3.3 Sensitivity analysis

We were interested in evaluating the impact in varying the segmentation parameters in the global error calculation. As mentioned in Section 2.2, we used the same parameters for the original object and RP model segmentation, except for λ_2 , which was the most sensitive one. We therefore did a sensitivity analysis varying each λ_2 in ± 10 percent and calculating the indexes A , *FP* and *FN* (Figures 13 and 14). We tested our results with the humerus data sets.

Changes in λ_2 for the RP model segmentation produced larger variations than for the object segmentation (Figure 14(c)). However, variations were always < 0.05 percent of the total volume of the original structure.

4. Discussion

We have developed a novel metric and a methodology for measuring the accuracy of RP models, specially suited for medical applications and with a reasonably degree of automation. Indeed, the entire evaluation process was done with minimal human intervention, which only required for the ellipsoid initialization of the segmentation process. The proposed indexes are a simple and meaningful way to observe the degree of global accuracy and the geometric errors of the built RP model. Moreover, as a complementary metric, we generated a local error representation that indicates how the error is distributed along the RP model surface. The results showed that both metrics were consistent.

For the construction of RP accuracy indexes it is necessary to establish correspondence between the objects of interest and their RP models. Until now alternative error metrics have faced such problem by trying to establish corresponding landmarks (sometimes referred as fiducials) on each structure and applying a rigid body (Euclidean) transformation to them.

Figure 8

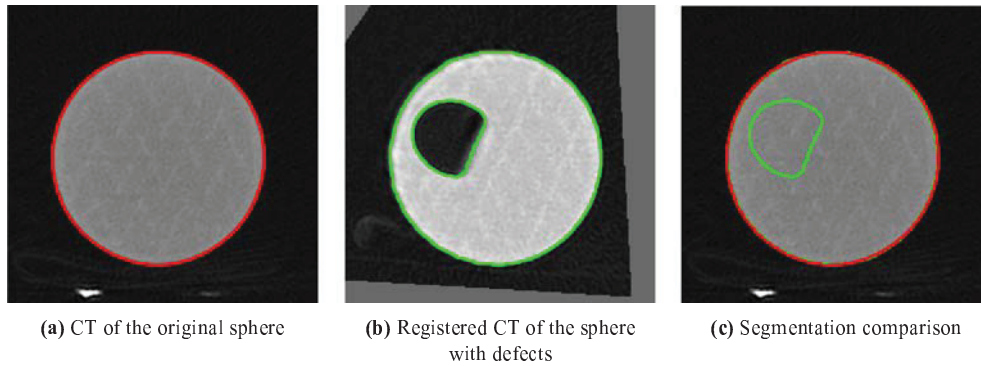


Figure 9

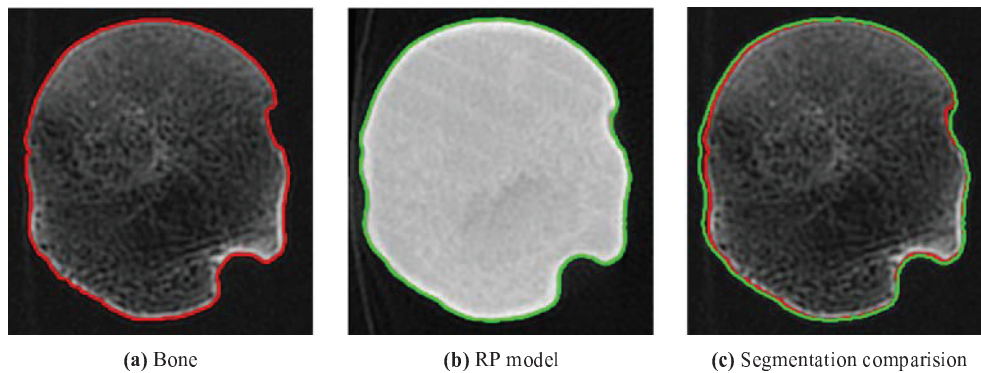
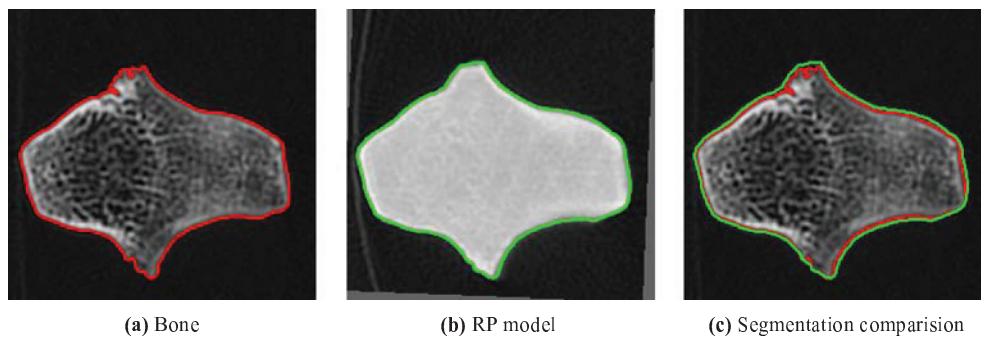


Figure 10



However, landmarking processes are labor-intensive and heavily depends on the ability of the operator to define those corresponding points (Maes *et al.*, 1997). In general, the resulting correspondence between external fiducials is poor (Meyer *et al.*, 1996). Furthermore, measuring a few landmarks does not give a good representation of the accuracy of complex shapes, and local representations of errors are needed (Germani *et al.*, 2010).

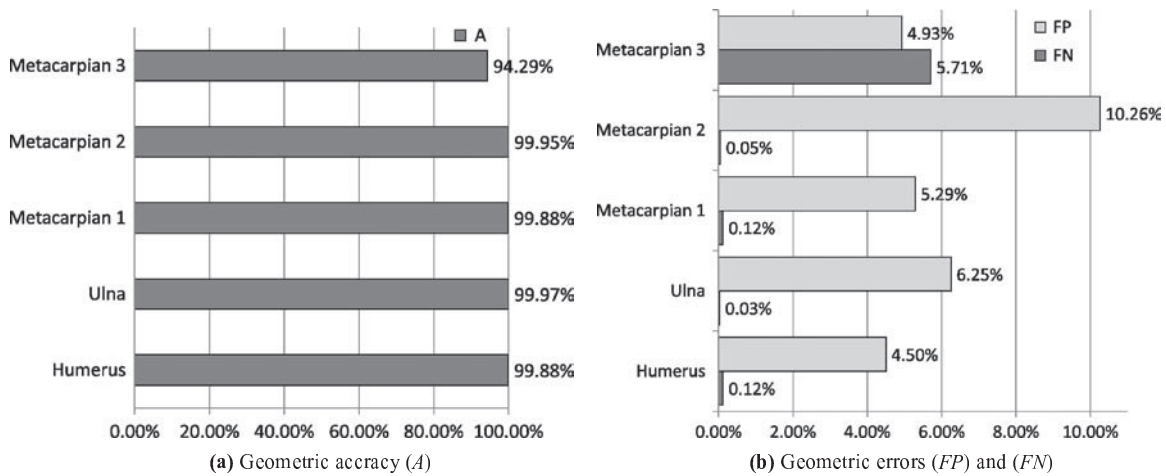
We propose an alternative solution, as there is substantial evidence that spatial correspondence can be better achieved by searching the rigid body transformation that maximizes the mutual information between images (Meyer *et al.*, 1996; Maes *et al.*, 1997). The method is robust even when there are intensity differences between the images that are

being registered. This is exactly our case as the image intensities of bones and RP models are shown differently in the CT scans.

An additional justification to move away from landmark-based error metrics, is their inherent ambiguity. As we showed (Figure 2), there are some situations where such metrics cannot not detect evident errors, they cannot discriminate the exact location of the errors or, depending where is measured, they show differently a single kind of error.

Another important issue is the chosen segmentation technique. Preliminary tests showed us that a significant portion of the geometric errors that we found in the RP models was produced by the thresholding-based segmentation algorithm. The threshold-based segmentations have the problem that Choi *et al.* (2002) called the dumb-bell-like effect.

Figure 11



Basically, choosing a smaller threshold than the ideal value adds a volume layer, whereas choosing a larger threshold than the correct one subtracts a volume layer. This is an inevitable drawback, especially in bone segmentation, since the detection of trabecular bone in most cases implies reducing the threshold and therefore an overestimation of cortical bone. In this scenario, we proposed the use of an active contour-based segmentation, which is semi-automatic, robust to the noise and combines geometric and intensity constraints. Thus, this method showed advantages compared to the threshold-based ones and allowed us to make a fair comparison between two structures that have different intensities.

From the computed results, it is interesting to observe that the RP models tended to overestimate the size of the original bone structure. In fact, the global accuracy indexes showed that *FP* were consistently greater than *FN*, except for the metacarpal 3. This might be due to the small size of this bone, particularly in the slice direction. This might increase the significance of the voxelation and volume averaging effects.

The local representation of error adds relevant information to geometric accuracy evaluations. The most important conclusions are two. On one hand, the amount of underestimated surface, i.e. the *FN* (see the color bars in the right side of Figure 12(a)-(F)) was usually concentrated in particular regions. On the other hand, the amount of overestimated surface, i.e. *FP* (surface of red color in Figure 12), was distributed along most of the surface, which confirms the results given by global indexes. An important contribution of our method is that it not only quantifies the error, but also shows where the error is located. This is an important issue for medical applications, such as surgery or prosthesis design, since geometric accuracy is particularly relevant at specific regions where the object interacts with other structures.

Similar local error representations could be achieved using CAD software that offer comparing tools for meshes (e.g. 3-Matic™ Materialise®, XOV™ Rapidform®). These software products typically use a point-based comparison between overlapped regions of two-point clouds and compute the distance between the nearest points from each cloud. However, using these solutions present three important restrictions. First, they do not integrate all the processes needed

for the accuracy evaluation (i.e. image-based registration, active contour-based segmentation, triangulation, indexes computation, local error computation and surface rendering), so additional software tools must be integrated. Second, a simple computation of the distance to the nearest point does not show information about the geometry and orientation of the error. It is necessary to define signed distances in order to discriminate between underestimated and overestimated errors. Third, measuring errors from point clouds works well for dense point distributions or when those points correspond to triangle vertices of similar triangulations (in terms of shape, smoothness and distribution). Otherwise, measurements are affected by point displacements, which are not necessarily geometric errors.

In this sense, our proposed method based on signed normal distances provides a more natural and general framework to analyze local geometric errors.

There are several sources that could explain the geometric errors found in the RP models: those derived from the scanning process (e.g. voxelation, volume averaging effects and reconstruction artifacts); those derived from the pre-processing stage (e.g. errors from the segmentation process, and from the surface triangulation); and those derived from the manufacturing process (e.g. miscalibration, voxelation effects and re-slice and building orientation). Our methodology also introduces additional sources of errors, such as potential misalignments obtained from the registration process, image interpolations involved in the registration process, and segmentation errors derived from the chosen segmentation algorithm (ACWE). However, the results with synthetic phantoms showed that these additional sources of errors were bounded and did not significantly affect our metric results. Indeed, the phantoms were built synthetically by software, so they did not contain errors from construction process (at least from the CT scan, segmentation and triangulation), and the computed error did not show significant differences with the synthetically introduced errors.

With our method for quantitative assessment of geometric errors we have the tools to judge the accuracy of eventual improvements for the construction process. In an image-processing context, we believe that efforts to improve the accuracy of RP models should be focused on the application of more adequate segmentation strategies to process the tomographic images of the original objects to be modeled.

Figure 12

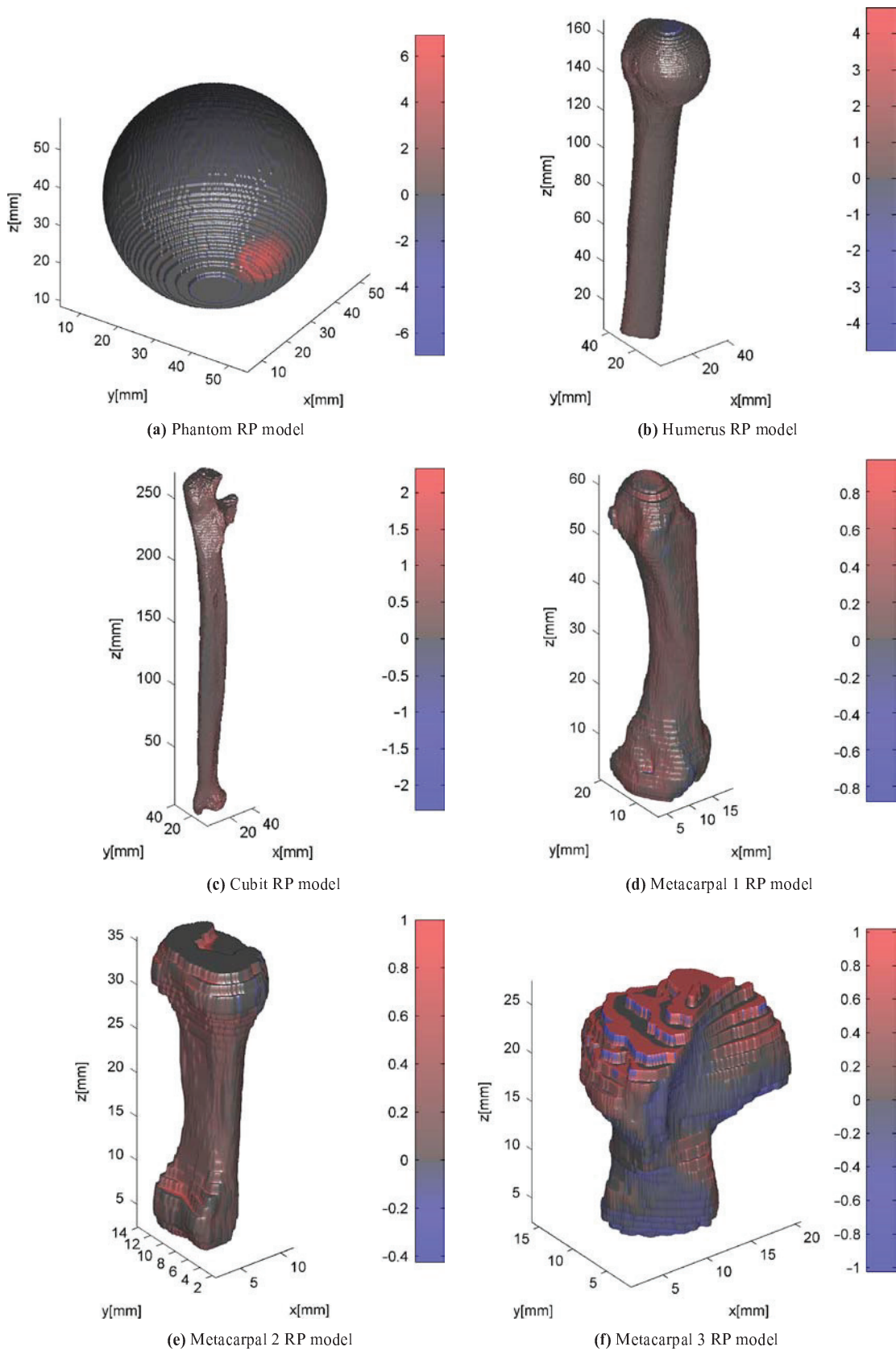
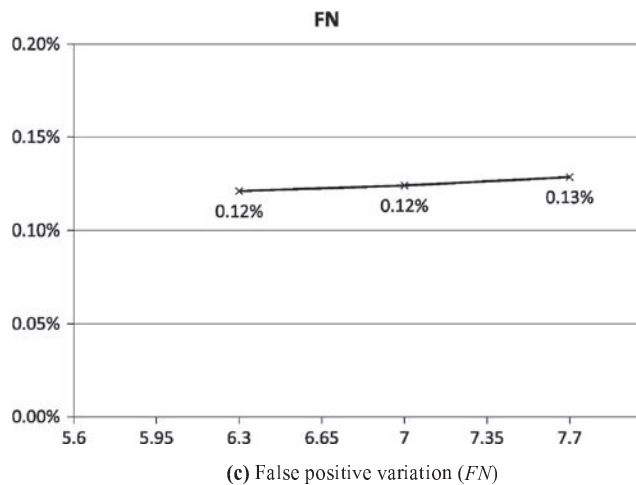
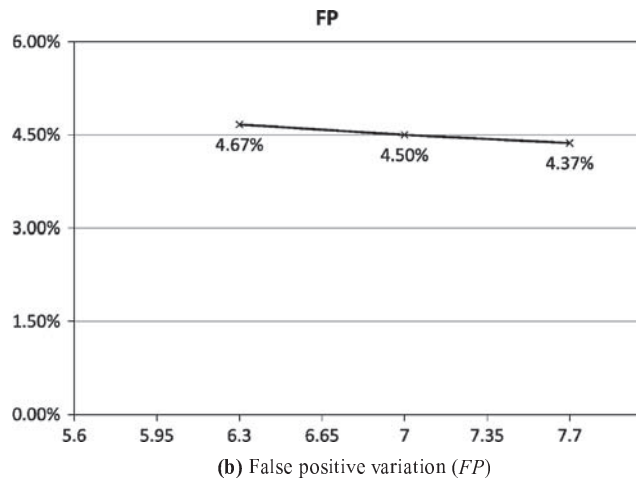
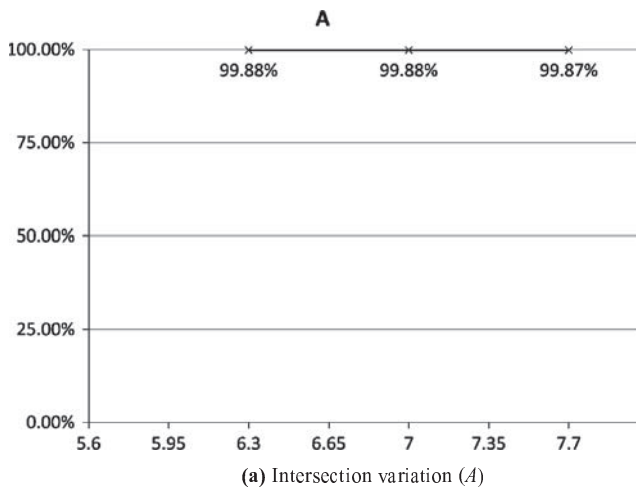
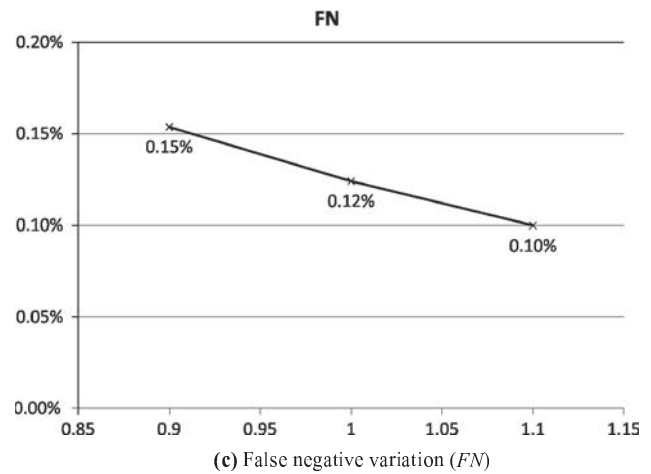
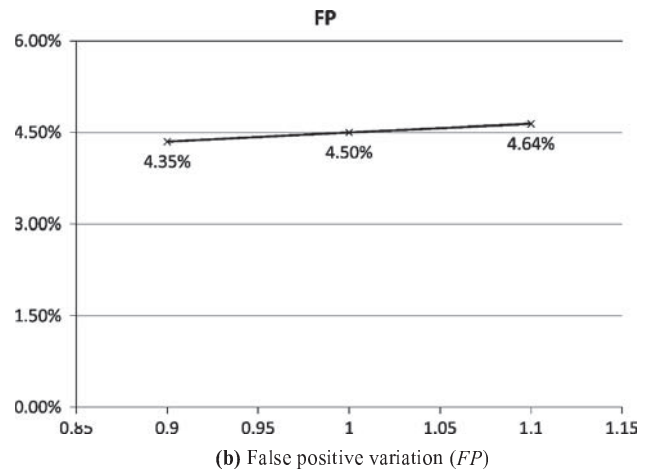
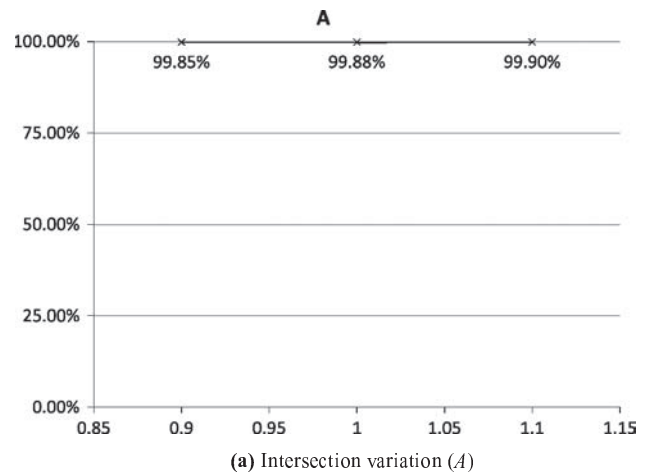


Figure 13



The segmentation tools available in standard RP software applications (thresholding and region growing) offer great advantages in terms of speed and simplicity, but they inevitably introduce segmentation errors. Indeed, they are not robust to noise and other commonly encountered artifacts in medical images. Denoising and smoothing filters are typically used to reduce this problem, with interesting results in term of

Figure 14



noise reduction. However, there is always a trade-off between noise content and image blurring, which are both potential sources of errors for standard segmentation algorithms. Additionally, those standard segmentation algorithms involve choosing heuristically some parameters (e.g. the magnitude of the thresholds), which potentially introduces biases as in medical imaging, the image contrast typically varies across the field of view due to image artifacts.

We are currently working on optimizing the codes, because of the high-computational costs. Indeed, the processing time varied from two hours for small data sets to 20 hours for the largest one. Particularly, the processing time that needs to be reduced is the local error metric time, which depends of the number of triangles of the object. We are also working on controlling the topology of the segmenting contour, such as in Han *et al.* (2003), so that to avoid the morphological corrections needed for the ACWE algorithm. This would simplify and improve robustness of the segmentation process.

References

- Chan, T. and Vese, L. (2001), "Active contours without edges", *IEEE Transaction on Image Processing*, Vol. 10, pp. 266-77.
- Choi, J., Choi, J., Kim, N., Kim, Y., Lee, J., Kim, M., Lee, J. and Kim, M. (2002), "Analysis of errors in medical rapid prototyping models", *International Journal of Oral and Maxillofacial Surgery*, Vol. 31, pp. 23-32.
- Ciocca, L., de Crescenzo, F., Fantini, M. and Scotti, R. (2009), "CAD/CAM and rapid prototyped scaffold construction for bone regenerative medicine and surgical transfer of virtual planning: a pilot study", *Computerized Medical Imaging and Graphics*, Vol. 33, pp. 58-62.
- El-Katatny, I., Masood, S. and Morsi, Y. (2010), "Error analysis of FDM fabricated medical replicas", *Rapid Prototyping Journal*, Vol. 16, pp. 36-43.
- Elkott, D. and Veldhuis, S. (2007), "CAD-based sampling for CMM inspection of models with sculptured features", *Engineering with Computers*, Vol. 23, pp. 187-206.
- Germani, M., Raffaelli, R. and Mazzoli, A. (2010), "A method for performance evaluation of RE/RP systems in dentistry", *Rapid Prototyping Journal*, Vol. 16, pp. 344-55.
- Han, X., Xu, C. and Prince, J.L. (2003), "A topology preserving level set method for geometric deformable models", *IEEE Transactions on Pattern Analysis and Machine Intelligence*, Vol. 25, pp. 755-68.
- Knox, K., Kerber, C., Singel, S., Bailey, M. and Imbesi, S. (2005), "Stereolithographic vascular replicas from CT scans: choosing treatment strategies, teaching, and research from live patient scan data", *American Journal of Neuroradiology*, Vol. 26, pp. 1428-31.
- Lorensen, W.E. and Cline, H.E. (1987), "Marching cubes: a high resolution 3D surface construction algorithm", *Computer Graphics*, Vol. 21, pp. 163-9.
- Maes, F., Collington, A., Vandermeulen, D., Marchal, G. and Suetes, P. (1997), "Multimodality image registration by maximization of mutual information", *Medical Image Analysis*, Vol. 16, pp. 187-98.
- Mallepre, T. and Bergers, D. (2009), "Accuracy medical RP models", *Rapid Prototyping Journal*, Vol. 5, pp. 325-32.
- Meakin, J., Shepherd, D. and Hukins, D. (2004), "Fused deposition models from CT scans", *The British Journal of Radiology*, Vol. 77, pp. 504-7.
- Meyer, C., Boes, J., Kim, B., Zasadny, P.B.K., Kison, P., Koral, K., Frey, K.A. and Wahl, R.L. (1996), "Demonstration of accuracy and clinical versatility of mutual information for automatic multimodality image fusion using affine and thin-plate spline warped geometric deformations", *Medical Image Analysis*, Vol. 1, pp. 195-206.
- Mumford, D. and Shah, J. (1989), "Optimal approximations by piecewise smooth functions and associated variational problems", *Communications on Pure and Applied Mathematics*, Vol. 42, pp. 577-685.
- Ngan, E., Rebeyka, I., Ross, D., Hirji, M., Wolfaardt, J., Seelaus, R., Grosvenor, A. and Noga, M.L. (2006), "The rapid prototyping of anatomic models in pulmonary atresia", *The Journal of Thoracic and Cardiovascular Surgery*, Vol. 132, pp. 264-9.
- Nizam, A., Gopal, R., Naing, L., Hakim, A. and Samsudin, A. (2006), "Dimensional accuracy of the skull models produced by rapid prototyping technology using stereolithography apparatus", *Orofacial Sciences*, Vol. 1, pp. 60-6.
- Russett, S., Major, P., Carey, J., Toogood, R. and Boulanger, P. (2007), "An experimental method for stereolith mandible fabrication and image preparation", *The Open Biomedical Engineering Journal*, Vol. 1, pp. 1-8.
- Schicho, K., Fogl, M., Seeman, R., Ewers, R., Lambrecht, J., Wagner, A., Watzinger, F., Baumann, A., Kainberger, F., Fruehwald, J. and Klug, C. (2006), "Accuracy of treatment planning based on stereolithography in computed assisted surgery", *Medical Physics*, Vol. 33, pp. 3408-17.
- Silva, D., de Oliveira, M., Meurer, E., Meurer, M., da Silva, J. and Santa Barbara, A. (2008), "Dimensional error in selective laser sintering and 3D-printing of models for craniomaxillary anatomy reconstruction", *Journal of Cranio-Maxillofacial Surgery*, Vol. 36, pp. 443-9.
- Wang, C., Wang, W. and Lin, M. (2010), "STL rapid prototyping bio-CAD model for CT medical image segmentation", *Computers in Industry*, Vol. 61, pp. 187-97.
- Wells, W., Viola, P. and Kikinis, R. (1996), "Multi-modal volume registration by maximization of mutual information", *Medical Image Analysis*, Vol. 1, pp. 35-51.

About the authors

Cristobal Arrieta obtained his BSc and MSc in Electrical Engineering at Pontificia Universidad Catolica de Chile, where he is currently a PhD student and where he is an Assistant Researcher in the Biomedical Imaging Center. His areas of interest are accuracy of rapid prototyping models in medical applications, image processing, segmentation, active contours and medical imaging. Cristobal Arrieta is the corresponding author and can be contacted at: ciarriet@uc.cl

Sergio Uribe obtained his PhD at King's College London. He took a position as an Assistant Professor in the Radiology Department and in the Biomedical Imaging Center at Pontificia Universidad Catolica de Chile, Santiago, Chile. His main research interests are medical imaging, translating new imaging methodology into clinical applications, magnetic resonance imaging, image processing and cardiovascular imaging.

Jorge Ramos-Grez is an Associate Professor of Mechanical Engineering at Pontificia Universidad Catolica de Chile and the Director and Founder of the Industrial Laser Manufacturing Technologies Laboratory (LATIL), Santiago, Chile. He currently is head of the Department and is interested in rapid prototyping of bone biomodels and biocompatible scaffolds for bone tissue engineering using adult mesenchymal stem cells.

Alex Vargas is an Associate Professor of the Medicine Faculty, Surgery Division, Oncologic and Maxillofacial Surgery Department at Pontificia Universidad Catolica de Chile, Santiago, Chile. He is interested in oral and maxillofacial implantology, traumatology, infection and malformations.

Pablo Irarrazaval graduated as an Electrical Engineer from the Pontificia Universidad Catolica de Chile (PUC) and obtained his MSc and PhD degrees from Stanford University. He is currently a Professor with the Department of Electrical Engineering at PUC. He is also the Director of the Biomedical Imaging Center of the same university. He is interested in medical imaging and particularly in magnetic resonance imaging.

Vicente Parot obtained his BSc and MSc in Electrical Engineering at Pontificia Universidad Catolica de Chile in 2009. He is currently part-time Professor of the Department

of Electrical Engineering and a Researcher at Biomedical Imaging Center at Pontificia Universidad Catolica de Chile, Santiago, Chile. His main research interests are magnetic resonance imaging, fractional Fourier transform, image reconstruction, and image processing.

Cristian Tejos received his BSc and MSc in Electrical Engineering in 2000 from the Pontificia Universidad Catolica de Chile. Shortly after, he moved to the UK to complete his academic training. First, he received a MSc degree from the Department of Bioengineering at Imperial College London. Second, he received a PhD degree from the School of Clinical Medicine at the University of Cambridge. In 2005, he returned to Chile and since then he has been Assistant Professor of the Department of Electrical Engineering and the Biomedical Imaging Center at Pontificia Universidad Catolica de Chile, Santiago, Chile. His main research interests are in image processing and medical imaging.